PHYSICAL REVIEW A, VOLUME 65, 032712

Excitation and alignment effects in Ar^{8+}-Cs$(6s,6p)$ collisions at low energies

V. Bazin,[1,2] P. Boduch,[1,2] M. Chantepie,[1,2] E. Jacquet,[1,2] H. Kucal,[1,2] and D. Lecler[1]
[1]*Centre Interdisciplinaire de Recherche Ions Lasers, UMR 6637 CEA-CNRS-ISMRA, Université de Caen, 6 Boulevard Maréchal Juin, F-14050 Caen Cedex, France*
[2]*UFR des Sciences, Université de Caen, F-14032 Caen Cedex, France*

J. Pascale
Service des Photons, Atomes et Molécules, CEA, Centre d'Etudes de Saclay, Bâtiment 522, F-91191 Gif-sur-Yvette Cedex, France

(Received 7 May 2001; published 14 February 2002)

The influence of the excitation and the alignment of a laser-prepared target on the final $n\ell m_\ell$ distributions are studied in Ar^{8+}-Cs$(6p\Sigma)$ and Ar^{8+}-Cs$(6p\Pi)$ collisions. These collisions are studied experimentally by means of near UV and visible photon spectroscopy (200–600 nm) in the 0.4–4.0 keV/amu energy range, and theoretically by using the three-body classical trajectory Monte Carlo (CTMC) method at 0.1–4.0 keV/amu. Calculations of electronic energies for the one-electron $\{Ar^{7+}\text{-Cs}\}^+$ molecular system have allowed an analysis of the results in terms of dynamical couplings. Polarization rates for single-electron-capture lines corresponding to transitions between high-ℓ values states are also measured. The comparison with those calculated from the CTMC results provides information about the magnetic sublevel distributions and the influence of the initial alignment of a laser-prepared target.

DOI: 10.1103/PhysRevA.65.032712 PACS number(s): 34.10.+x, 34.70.+e

I. INTRODUCTION

In a previous paper [1], we studied Ar^{8+}-Cs$(6s)$ collisions at low energies (0.4–5.0 keV/amu) by UV and visible photon spectroscopy. In this energy range, the main process that occurs is the capture of the active loosely bound electron of the target by the incident ion with a large cross section [2,3]. We determined the $n\ell$ distributions of the most populated levels of the Ar^{7+} ions. The measurements of the polarization rates of the single-electron-capture lines and the comparison with the polarization degrees calculated from $\sigma(n\ell m_\ell)$ cross sections determined by using the classical-trajectory Monte Carlo (CTMC) method [4–6] allowed us to have information on the m_ℓ distributions. The knowledge of the final $n\ell$ and $n\ell m_\ell$ distributions gives information on the importance of the various mechanisms that take place during the collision. In the present paper, we study the effects of the initial alignment of a laser-prepared target on the final $n\ell$ and $n\ell m_\ell$ distributions: the cesium atoms are excited in the $6p\Sigma$ and $6p\Pi$ aligned states, i.e., the electronic orbital cloud is, respectively parallel and perpendicular to the incident ion beam (Fig. 1).

Some systems with laser-prepared target have already been studied. Most of them concern low-charged projectiles [Na^+-Na$(3p)$ [7,8], H^+-Na$(3p)$ [9,10], He^+-Na$(3p)$ [11], He^{2+}-Na$(3p)$ [12–15], He^{2+}-Li$(2p)$ [16,17] and Ar^{2+}, Ne^{2+}-Na$(3p)$ [18]]. However, some studies have been realized with highly charged ions, Ar^{7+}-Na$(3p)$ [19,20], O^{8+}-Na$(3p)$ [21], and C^{4+}-Na$(3p)$ [22]. These works allowed us to determine the $\sigma_i(n)$ and/or $\sigma_i(n,\ell)(i\equiv\Sigma,\Pi)$ cross sections and showed an important anisotropy, characterized by the parameter A defined by

$$A=\frac{\sigma_\Sigma-\sigma_\Pi}{\sigma_\Sigma+\sigma_\Pi}. \qquad (1)$$

The anisotropy parameter A depends on the projectile velocity [23–25] and on the size and the charge of the projectile [22]. In order to study the influence of these parameters, not only on the $n\ell$ distributions but also on the $n\ell m_\ell$ distributions when the target is prepared in an excited state, we have chosen to extend our previous work on the Ar^{8+}-Cs$(6s)$ system to the study of the Ar^{8+}-Cs$(6p\Sigma)$ and Ar^{8+}-Cs$(6p\Pi)$ systems. Apart from the fact that the cesium atom is an alkali atom such as lithium or sodium atoms, the choice of a cesium target is purely technical. Indeed, the marketing of power single-mode laser diode working at 852 nm, i.e., corresponding to the $6s$-$6p$ caesium transition, allowed us to realize a compact laser excitation setup.

In this paper, we present the results obtained for collision energies from 0.1 to 4.0 keV/amu. After a brief outline of the experimental setup, we describe in details the optical preparation of the cesium target. We explain on one hand, how the excited cesium fraction is determined and on the other hand, how fine and hyperfine effects are taken into account. Since the CTMC method was already described in our previous study [Ar^{8+}-Cs$(6s)$ collisions [1]], we just outline it here, laying emphasis on the determination of the initial conditions

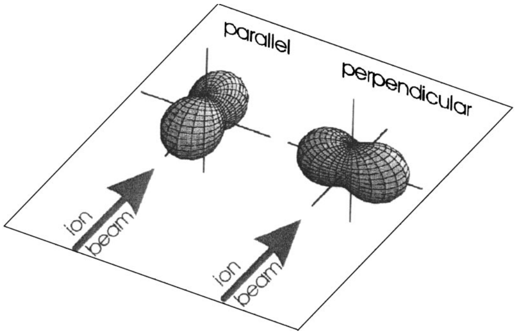

FIG. 1. Spatial alignment of charge cloud versus laser polarization.

1050-2947/2002/65(3)/032712(14)/$20.00

for Cs target excited and aligned in the $6p\Sigma$ or $6p\Pi$ states. After this presentation, we report experimental results, in particular, spectroscopic results, emission cross sections, and polarization rates of single-electron-capture lines corresponding to transitions between high-ℓ values. The experimental emission cross sections and polarization rates are compared with the calculated CTMC ones. In particular, comparisons between experimental and CTMC calculated polarization rates give information on the $n\ell m_\ell$ distributions versus the collision energy. Finally, the dynamics of the collision is analyzed from calculations of electronic potential-energy curves for the $\{\mathrm{Ar}^{7+}\text{-}\mathrm{Cs}\}^+$ molecular system.

II. EXPERIMENT

A. General features of the experimental setup

The experimental setup used to study the collisions between Ar^{8+} ions and a pure $\mathrm{Cs}(6s)$ ground-state target has already been described in a previous work [1]. The ion beam is produced by an ECR source of the GANIL (Grand Accélérateur National d'Ions Lourds, Caen, France). After a q/m selection, the Ar^{8+} ions are focused inside a collision chamber on a well-collimated jet of cesium atoms. The cesium beam whose direction is at 45° from the Ar^{8+} ion beam is produced in an oven. In the opposite direction, a movable Langmuir-Taylor detector [14,26] is used to measure the atomic caesium beam density (10^9 atoms per cm^3).

A decelerating device was installed at the vicinity of the collision area in order to investigate the low-energy range (0.4–4.0 keV/amu) [27].

The photons emitted in $\mathrm{Ar}^{8+}\text{-}\mathrm{Cs}(6s,6p)$ collisions are detected perpendicularly to the direction of the incident ion beam. They are wavelength selected by a normal incidence grating spectrometer and detected by a photomultiplier in the (200–600)-nm wavelength range. Emission cross sections of ArVIII lines are determined from photonic spectra. In order to measure the intensity of the emitted light polarized along ($I_\parallel$) or perpendicular ($I_\perp$) to the ion beam, a polarimeter is installed in front of the entrance slit of the spectrometer. It is composed of two polarizers: a rotating Polacoat whose polarization direction can be oriented parallel or perpendicular to the direction of the ion beam and a fixed Glan-Taylor prism that compensates for the polarization effects of the spectrometer (grating and mirror). The polarization degree P of the emitted lines is determined from the direct measurements of $I_\parallel$ and $I_\perp$ and is defined by

$$P=\frac{I_\parallel-I_\perp}{I_\parallel+I_\perp}. \tag{2}$$

B. Optical preparation of the cesium target

In our experiment, we are only interested in the $6s^2\mathrm{S}_{1/2}\rightarrow 6p^2\mathrm{P}_{3/2}$ transition whose wavelength is equal to 852 nm. The caesium has a nuclear spin $I=\frac{7}{2}$. The $6s^2\mathrm{S}_{1/2}$ and $6p^2\mathrm{P}_{3/2}$ fine levels are split into hyperfine levels (Fig. 2). Initially, the population is distributed statistically among the fundamental hyperfine levels: 44% for the $6s^2\mathrm{S}_{1/2}(F=3)$ level and 56% for the $6s\,^2S_{1/2}(F=4)$ level. In order to optimize the number of excited cesium atoms, both hyperfine fundamental levels have to be pumped in the $6p$ configuration. Note also that the pumping of these two levels allows to cast off the trapping effect [28] that can reduce the excited caesium fraction. As a consequence, two pumping frequencies are needed. Two powerful single-mode distributed Bragg reflector laser diodes (SDL 5712 H1 and SDL 5722 H1) were then used to pump the $6s\,^2S_{1/2}(F=3)\rightarrow 6p\,^2P_{3/2}(F=3)$ and $6s\,^2S_{1/2}(F=4)\rightarrow 6p\,^2P_{3/2}(F=5)$ transitions since no electro-optical modulator inducing sidebands on the primary frequency of a laser works at 9193.3 MHz [23] (see Fig. 2). The laser light is linearly polarized and crosses both ion and caesium beams at right angles.

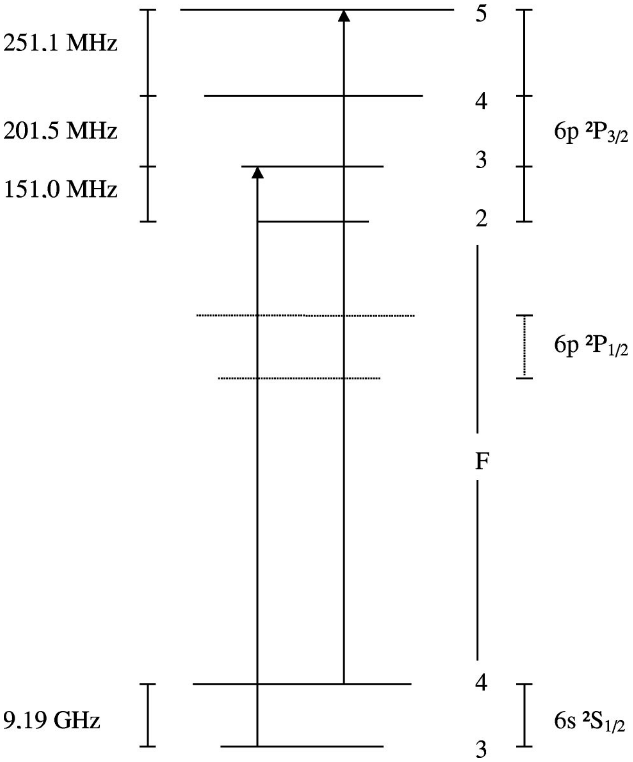

FIG. 2. Hyperfine splitting of the $6s\,^2S_{1/2}\rightarrow 6p\,^2P_{3/2}$ transition.

At the operating temperature (300 K), the Doppler broadening of a hyperfine line is about 380 MHz and then is upper than the gap between two successive hyperfine levels of the excited state [29] (Fig. 2). In these conditions, a saturated absorption setup has been used to resolve the hyperfine splitting of the $6p^2\mathrm{P}_{3/2}$ level [30]. An example of saturated absorption profile is shown in Fig. 3. The observed dips are called Lamb dips and correspond either to hyperfine transitions or crossover [30]. Since the laser linewidth (3 MHz) is very weak, the dip width corresponds mainly to the natural $\mathrm{Cs}(6p)$ linewidth (about 30 MHz) [31].

Finally, each laser frequency is locked to one of both hyperfine transitions so that the pumping may be efficient. The principle consists first in modulating at low frequency (373 Hz in our case) the detected saturated absorption signal around the Lamb dip corresponding to the cesium $6s\,^2S_{1/2}(F=3)\rightarrow 6p\,^2P_{3/2}(F=3)$ or $6s\,^2S_{1/2}(F=4)\rightarrow 6p\,^2P_{3/2}(F=5)$ transition. Then the signal is derived by

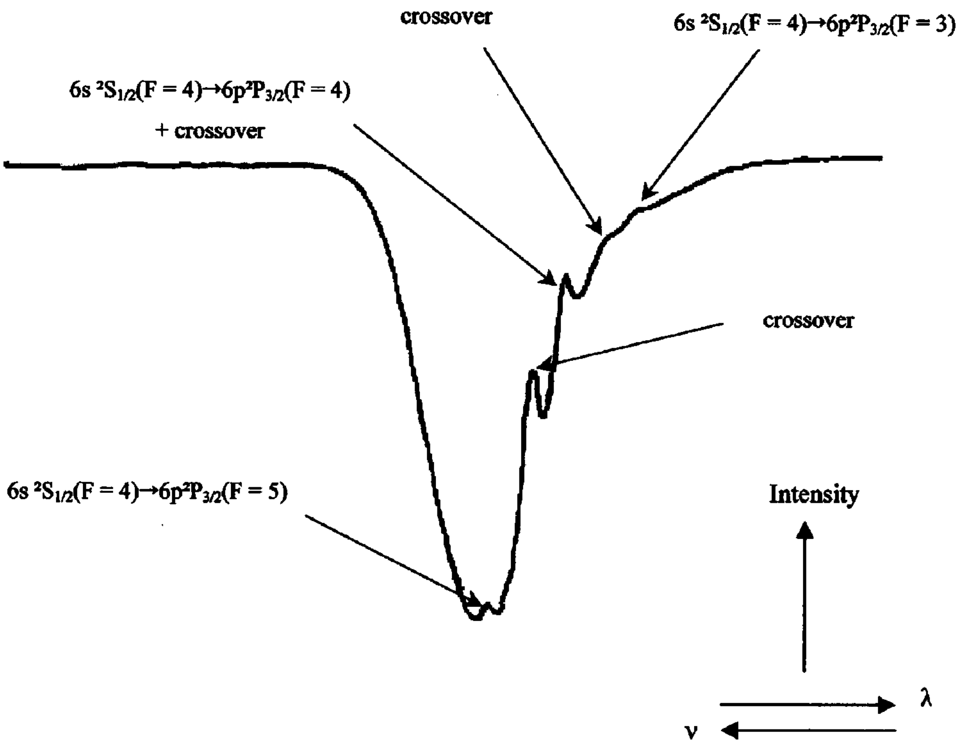

FIG. 3. Experimental saturated absorption profile.

using a lock-in amplifier. As the obtained curve is asymmetrical and changes sign, an integrator is used to cancel the derived signal that corresponds to the maximum of the Lamb dip.

C. Determination of the excited cesium fraction

The target beam is composed of atoms in the ground state and in the excited state because the cesium atoms are not all excited in the $6p$ state. The average excited cesium fraction is defined by the ratio between the excited-state density and the total cesium density. The recorded photonic spectra are due to Ar^{8+}-Cs($6s$) and Ar^{8+}-Cs($6p$) collisions. The $\sigma_{6s,6p}$ emission cross section is, therefore, expressed as

$$\sigma_{6s,6p}=\overline{f}\sigma_{6p}+(1-\overline{f})\sigma_{6s}, \tag{3}$$

where σ_{6s} is the emission cross section with cesium atoms in the ground state and σ_{6p} the emission cross section with cesium atoms in the $6p$ excited state.

The excited fraction $\overline{f}$ is determined from the laser-induced deflection of the cesium beam and the results obtained previously by Schlatmann [14] in He^{2+}-Na($3s$,$3p$) collisions. The average excited cesium fraction $\overline{f}$ can then be determined by the following formula:

$$\overline{f}<\frac{\overline{v}\,\overline{d}}{Nv_0}, \tag{4}$$

where $\overline{v}$ is the average velocity of the cesium beam, $\overline{d}$ the average deflection due to the radiation pressure of the laser, N the maximum number of excitation cycles, and v_0 the velocity change by the absorption of one photon. The deflection is determined by recording two Langmuir-Taylor profiles with laser "off" and laser "on" (Fig. 4). Generally, the average excited cesium fraction is about 10%.

The weak fraction may be explained by the vertical Doppler effect due to the laser-beam divergence. It is about 24 MHz and is more or less equal to the natural Cs($6p$) linewidth. It is, therefore, possible that the outputs of the laser diodes are not tuned to the corresponding hyperfine transitions and contribute to decrease the excited cesium fraction. Note that the earth magnetic-field effect is too weak to detune the laser diodes. At best, it is equal to 3 MHz. It is not necessary to compensate for it.

D. Fine and hyperfine coupling effects

The laser polarization and then the Cs($6p$) charge cloud can be aligned parallel or perpendicular to the ion beam by

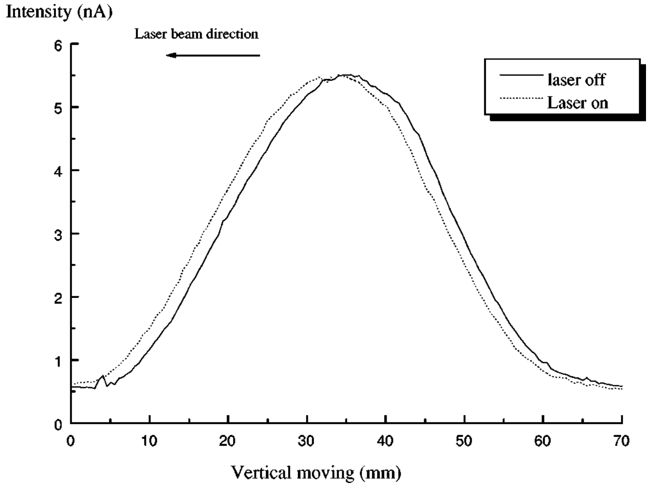

FIG. 4. Langmuir-Taylor profile with laser "off" and laser "on."

using a half wave plate (Fig. 1). However, due to the fine and hyperfine couplings effects, a target polarized parallel (respectively perpendicular) to the ion beam does not correspond to a target prepared in the $6p\Sigma$ state (respectively $6p\Pi$ state) but only to a target polarized in majority in the $6p\Sigma$ state (respectively $6p\Pi$ state). Thus, to compare experiment and theory, $\sigma_{6p\Sigma}$ and $\sigma_{6p\Pi}$ cross sections have been expressed as function as $\sigma_{6p}^{\parallel}$ and $\sigma_{6p}^{\perp}$ cross sections by using the alignment parameter formalism. The alignment parameter of the $\mathrm{Cs}(6pm_\ell)$ target is expressed as [32]

$$a_0=\sum_{-\ell}^{+\ell}[3m_\ell^2-\ell(\ell+1)]\rho_{m_\ell} \tag{5}$$

with $\ell=1$ for a p state. This parameter is calculated in the photon frame in which the quantization axis is parallel to the polarization vector of the laser light. In the stationary conditions, $a_0=-\frac{10}{17}$ that corresponds to $\rho_0=\frac{9}{17}$ and $\rho_{\pm1}=\frac{4}{17}$.

For a comparison with the theory, the populations have to be expressed in the collision frame in which the quantization axis is chosen parallel to the ion beam. Because of the axial symmetry of the collision system, both orbitals perpendicular to the ion beam axis are equivalent and are summed to form an orbital called Π. The third orbital that is parallel to the ion beam is denoted Σ. The population of $6p\Sigma$ and $6p\Pi$ orbitals can be calculated in the collision frame in terms of ρ_0 and $\rho_{\pm1}$ populations.

When the electric vector is parallel to the ion beam axis

$$\rho_{6p\Pi}^{\parallel}=\rho_{-1}+\rho_1=\frac{2}{3}+\frac{a_0}{3} \tag{6}$$

and

$$\rho_{6p\Sigma}^{\parallel}=\rho_0=\frac{1}{3}-\frac{a_0}{3}. \tag{7}$$

When the electric vector is perpendicular to the ion beam axis

$$\rho_{6p\Pi}^{\perp}=\rho_{-1}+\rho_0=\frac{2}{3}-\frac{a_0}{6} \tag{8}$$

and

$$\rho_{6p\Sigma}^{\perp}=\rho_1=\frac{1}{3}+\frac{a_0}{6}. \tag{9}$$

The $\sigma_{6p}^{\parallel}$ and $\sigma_{6p}^{\perp}$ measured cross sections are then expressed in terms of $\sigma_{6p\Sigma}$ and $\sigma_{6p\Pi}$ cross sections. Finally, the formulas are easily transformed to corresponding $\sigma_{6p\Sigma}$ and $\sigma_{6p\Pi}$ cross sections via

$$\sigma_{6p\Sigma}=\frac{26}{10}\sigma_{6p}^{\parallel}-\frac{16}{10}\sigma_{6p}^{\perp} \tag{10}$$

and

$$\sigma_{6p\Pi}=-\frac{8}{10}\sigma_{6p}^{\parallel}+\frac{18}{10}\sigma_{6p}^{\perp}. \tag{11}$$

III. CTMC CALCULATIONS

Details of the three-body CTMC method have already been given in our paper on Ar^{8+}-$\mathrm{Cs}(6s)$ collisions [1], where the parameters of the model potentials used to describe the interactions between the active electron and the Cs^{+} and Ar^{8+} cores were reported. For the Ar^{8+}-$\mathrm{Cs}(6p)$ collision, the binning procedure of the relevant classical quantities to determine the final n, $n\ell$, and $n\ell m_\ell$ distributions remains identical. Nevertheless, in the case of a $^2\mathrm{P}$ aligned target, the initial conditions for the excited and aligned target must be carefully examined. As usual [4], once the electronic energy of the $\mathrm{Cs}(6p)$ is given (the energy splitting of the fine-structure levels can be neglected), the initial classical orbit of the active electron about the core target is pseudorandomly determined from a microcanonical distribution by using the method of Reinhold and Falcón [33]. In addition, the initial orbital quantum number ℓ is specified by the classical angular momentum $\mathbf{L}_c$ and the condition

$$\ell\leqslant L_c<\ell+1 \tag{12}$$

with $\ell=1$. For a ^2P aligned target, a collision plan must be specified. The collision plan is chosen to be *OXZ*, with *OZ* parallel to the incident ion beam. Then, since the laser light is linearly polarized, we proceed as it follows to determine the Σ and Π symmetry states of the target. The quantization axis is chosen successively among *OX*, *OY*, and *OZ*. For each choice *OZ* of the quantization axis, the electronic cloud will be parallel to this axis if the projection L_c^z of $\mathbf{L}_c$ verifies the condition

$$\frac{2m_\ell-1}{2\ell+1}\leqslant L_c^z<\frac{2m_\ell+1}{2\ell+1} \tag{13}$$

with $m_\ell=0$. Thus, the choice *OZ* as quantization axis with the condition (13) defines the electronic cloud of the initial orbit to be parallel to the incident ion beam, the initial orbital is denoted Σ. For the choice *OX*, the electronic cloud is perpendicular to the incident ion beam, in the collision plan, the initial orbital is denoted Π^{+}. Finally, for the choice *OY*, the electronic cloud is perpendicular to the incident ion beam and perpendicular to the collision plan, the initial orbital is denoted Π^{-}. For each choice of the quantization axis, the Hamilton's equations are solved and the corresponding state-selective cross sections σ_{Σ}, $\sigma_{\Pi^{+}}$, and $\sigma_{\Pi^{-}}$ are determined. For each calculation, between 5×10^4 and 2.5×10^5 trajectories have been used to ensure final $n\ell$ distributions with statistical errors of 3–10% for the most populated levels ($n=11$, 12, 13, and 14) while the $n\ell m_\ell$ distributions have statistical errors of 8–20% for the most populated $n\ell$ sublevels. However, because the experiment cannot specify the orientation of the electronic cloud perpendicular to the incident ion beam, we define an averaged cross section

$$\sigma_{\Pi}=\frac{\sigma_{\Pi^{+}}+\sigma_{\Pi^{-}}}{2} \tag{14}$$

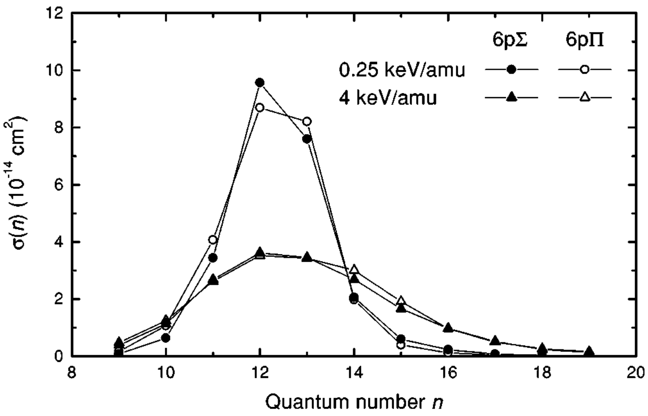

FIG. 5. CTMC calculated cross section at projectile energies of 0.25 keV/amu (circles) and 4 keV/amu (triangles) for electron capture into n levels of Ar^{7+} from $Cs(6p\Sigma)$ (full symbols) and $Cs(6p\Pi)$ (open symbols).

corresponding to an initial orbital Π. The CTMC calculations have been performed in the 0.1–4 keV/amu energy range.

For comparison with the experimental data, line-emission cross sections have been calculated from cross sections for electron capture into the $n\ell$ sublevels. Transitions probabilities calculated by Lindgård and Nielsen [34] for states with $\ell \leqslant 4$, otherwise hydrogenic transition probabilities, have been used in the calculations that take also into account possible cascading radiative transitions from high $n\ell$ levels (up to $n=20$). Details of the calculation of polarization rates from CTMC calculated $n\ell m_\ell$ cross sections can be found in Refs. [38], [40]. The calculation of the polarization rates includes radiative cascade effects up to $n=14$.

Before presenting the experimental results, it is worth noting that the CTMC calculated total electron capture into Ar^{7+} from $Cs(6p)$ are about a factor 2 larger than from $Cs(6s)$. Also, while the electron capture from $Cs(6s)$ is predominantly into the $n=10$ level for the low energies and also into the $n=11$ level at 4 keV/amu [1], it is predominantly into the $n=12$ and 13 levels from a $Cs(6p)$ target at low energies, the n distribution broadening much at large energies. This can be seen in Fig. 5, where the influence of the alignment of the excited state is shown to be negligible.

TABLE I. The observed lines (1) HFR calculations, (2) present experimental results.

Transition	Wavelength (nm) in vacuum (1)	Wavelength (nm) in air (2)
$10i$-$13k$	348.72	
$10k$-$13l$	348.74	348.64± 0.08
$10l$-$13m$	348.73	
$10m$-$13n$		
$11k$-$13l$	606.62	
$11l$-$13m$	606.59	606.49± 0.16
$11m$-$13n$		
$11n$-$13o$		
$11k$-$14l$	450.24	
$11l$-$14m$	450.24	450.04± 0.08
$11m$-$14m$	450.25	
$11n$-$14o$	450.25	

IV. EXPERIMENTAL RESULTS AND COMPARISONS WITH CTMC CALCULATIONS

A. Spectroscopic results

The recorded photonic spectra correspond to a mixture of Ar^{8+}-$Cs(6s)$ and Ar^{8+}-$Cs(6p)$ systems. Most of the observed lines due to the single-electron-capture process were already identified in a previous work [1]. However, three more lines corresponding only to transitions between high-ℓ values states have been identified in the (200–600)-nm wavelength range by using theoretical data obtained from spectroscopic *ab initio* pseudorelativistic Hartree-Fock calculations [35]. These lines are presented in Table I. They correspond to $\Delta n=2$ to 3 transitions from $n=13$ and 14. As already noticed above, as the $6p$ electron is less bound than the $6s$ one, the reaction window for electron capture from $Cs(6p)$ is shifted towards higher n values centered around $n=12$. Among these lines, only $11k,l,m,n$-$14l,m,n,o$ transitions are clearly identified. The two other lines are superposed unfortunately with lines already observed in Ar^{8+}-$Cs(6s)$ collisions. Nevertheless, taking into account the increase of each line intensity and the identification of $11k,l,m,n$-$14l,m,n,o$ transitions, one can assume that $10i,k,l,m$-$13k,l,m,n$ and $11k,l,m,n$-$13l,m,n,o$ transitions are respectively superposed with $9h,i,k,l$-$11i,k,l,m$ and

TABLE II. Experimental emission cross sections (10^{-16} cm²) versus projectile energy (keV/amu) for single electron capture in Ar^{8+}-$Cs(6p\Sigma)$ collisions.

Energy $n\ell$-$n'\ell'$	0.4	1.0	2.0	3.0	4.0
$9h,i,k,l$-$11i,k,l,m$ + $10i,k,l,m$-$13k,l,m,n$	245.7± 122.9	191.0± 95.5	269.7± 134.9	416.7± 208.4	241.3± 120.7
$9h,i,k,l$-$12i,k,l,m$	190.9± 103.1		176.2± 95.1	146.7± 79.2	3.8± 68.6
$10i,k,l,m$-$12k,l,m,n$	232.9± 116.5			216.3± 108.2	
$11k,l,m,n$-$14l,m,n,o$	19.3± 9.7		58.2± 29.1	30.7± 15.4	38.0± 19.0

TABLE III. Experimental emission cross sections (10^{-16} cm^2) versus projectile energy (keV/amu) for single electron capture in Ar^{8+}-Cs($6p\Pi$) collisions.

Energy $n\ell$-$n'\ell'$	0.4	1.0	2.0	3.0	4.0
$9h,i,k,l$-$11i,k,l,m$ + $10i,k,l,m$-$13k,l,m,n$	208.3 ± 104.2	263.4 ± 132.7	250.6 ± 125.3	356.5 ± 178.3	44.8 ± 22.4
$9h,i,k,l$-$12i,k,l,m$	63.8 ± 31.9		104.1 ± 52.1	109.7 ± 54.9	107.5 ± 53.8
$10i,k,l,m$-$12k,l,m,n$	264.4 ± 132.2			249.3 ± 124.7	310.4 ± 155.2
$11k,l,m,n$-$14l,m,n,o$	31.2 ± 15.6		59.7 ± 29.9	57.5 ± 28.8	67.6 ± 33.8

$9i,k,l-10k,l,m$ transitions. A further checking of the identification of the lines has been made also from relativistic semiempirical pseudopotential calculations [36].

B. Emission cross sections

The experimental emission cross sections of the main observed lines are reported in Tables II and III for projectile energies between 0.4 and 4.0 keV/amu. They correspond respectively to transitions between high-ℓ values states in Ar^{8+}-Cs($6p\Sigma$) and Ar^{8+}-Cs($6p\Pi$) collisions. They are determined from line intensities, the cesium density, and the optical response of the experimental device for each transition. As the efficiency curve of the grating photomultiplier couple is known in relative value, experimental emission cross sections are calculated from a reference cross section [$\sigma(3s6h\ {}^1H_5$-$3s7i\ {}^1I_5)$ in Ar^{8+}-He($1s^2$) collisions at 3.0 keV/amu] [37]. Moreover, as the resolution of our optical device is not sufficient to resolve these groups of transitions, the individual emission cross sections are not determined. However, we can note that the individual emission cross sections might be deduced from the emission cross section of the unresolved structure and the CTMC intensity ratios obtained from the CTMC calculated emission cross sections (assuming the CTMC results are sufficiently accurate). We can also notice that the determination of the electron-capture cross sections from the experimental data should not give more information. Indeed, radiative cascades have little effect on the most populated states (12ℓ and 13ℓ), the determination of the electron-capture cross sections would be then equivalent to duplicate the CTMC results. Therefore, it is justified to discuss only the emission cross sections. Except for two cases (the emission cross sections for the $9h,i,k,l$-$12i,k,l,m$ group of lines at 1.0 and 4.0 keV/amu), the relative uncertainties are about 50%. They are mainly due to the uncertainty about the reference emission cross section, the quality of the spectra, and the uncertainty about the excited cesium fraction.

The individual CTMC calculated emission cross sections are reported in Tables IV and V for the only lines corresponding to transitions observed experimentally with a target prepared in a Σ or Π state. For each group of transitions, they are summed for direct comparisons with the experimental results (Tables II and III). For three examples, the comparisons between experimental and CTMC calculated emission cross sections as functions of the projectile energy are shown in Figs. 6(a)–6(c). On the whole, the CTMC calculations are found in good agreement with the experimental results, taking the large experimental uncertainties into consideration. Nevertheless a few disagreements we do not explain are observed at 4.0 keV/amu. Thus, we note an important difference between the $\sigma_{6p\Sigma}$ and $\sigma_{6p\Pi}$ experimental cross sections that behave randomly in accordance with the lines. Note also that no experimental result is shown at 1.0 keV/amu because of the bad quality of the spectra for this energy. Apart from these disagreements, the $\sigma_{6p_i}(9\ell$-$12\ell')$,

TABLE IV. CTMC emission cross sections (10^{-16} cm^2) versus projectile energy (keV/amu) for single electron capture in Ar^{8+}-Cs($6p\Sigma$) collisions.

	Energy						
Transition	0.1	0.25	0.5	1.0	2.0	3.0	4.0
$9h$-$11i$	11.0	10.7	11.3	10.8	11.9	15.1	14.4
$9i$-$11k$	26.9	28.6	28.3	28.0	34.9	36.0	31.7
$9k$-$11l$	47.6	58.8	58.9	61.5	67.3	63.8	55.3
$9l$-$11m$	60.6	86.1	85.2	93.8	92.5	83.7	78.4
Sum1	146.1	184.2	183.7	194.1	206.6	198.6	179.8
$10i$-$13k$	14.6	11.7	9.4	7.3	6.4	6.7	6.6
$10k$-$13l$	20.0	18.3	15.9	13.1	14.9	14.6	11.5
$10l$-$13m$	20.8	23.3	20.7	18.8	24.9	21.5	16.0
$10m$-$13n$	11.5	16.0	15.6	17.7	20.4	19.1	15.5
Sum2	66.9	69.3	61.6	56.9	66.6	61.9	49.6
Sum1 + Sum2	213.0	253.5	245.3	251.0	273.2	260.5	229.4
$9h$-$12i$	12.0	11.0	9.5	8.2	7.4	7.9	6.9
$9i$-$12k$	22.6	20.4	19.9	16.2	18.6	18.8	16.2
$9k$-$12l$	31.1	31.9	30.2	27.7	32.7	31.0	25.5
$9l$-$12m$	23.8	28.8	27.5	29.2	30.6	27.9	23.8
Sum	89.5	92.10	87.1	81.3	89.3	85.6	72.4
$10i$-$12k$	21.9	19.9	19.3	15.7	18.1	18.3	15.8
$10k$-$12l$	38.9	39.9	37.7	34.6	40.8	38.7	31.9
$10l$-$12m$	50.8	61.6	58.9	62.4	65.4	59.6	50.9
$10m$-$12n$	50.7	71.6	68.5	73.9	73.9	65.1	63.1
Sum	162.3	193.0	184.4	186.6	198.2	181.7	161.7
$11k$-$14l$	3.6	4.9	5.1	4.5	5.1	6.1	5.7
$11l$-$14m$	3.4	5.8	6.7	6.3	9.4	9.8	7.5
$11m$-$14n$	2.5	5.1	6.9	8.6	12.0	10.7	9.2
$11n$-$14o$	1.3	2.7	4.2	6.6	9.4	7.9	8.1
Sum	10.8	18.5	22.9	26.0	35.9	34.5	30.5

TABLE V. CTMC emission cross sections (10^{-16} cm^2) versus projectile energy (keV/amu) for single electron capture in Ar^{8+}-Cs($6p\Pi$) collisions.

	Energy						
Transition	0.1	0.25	0.5	1.0	2.0	3.0	4.0
$9h$-$11i$	11.9	11.7	11.8	10.2	11.0	11.7	10.2
$9i$-$11k$	27.7	30.2	30.6	28.5	32.8	30.0	25.4
$9k$-$11l$	48.6	60.6	63.9	68.7	73.0	63.7	53.3
$9l$-$11m$	58.8	84.9	92.3	111.1	111.0	98.8	87.2
Sum1	147.0	187.4	198.6	218.5	227.8	204.2	176.1
$10i$-$13k$	12.4	12.7	11.6	8.2	7.1	6.8	5.6
$10k$-$13l$	18.6	20.5	19.0	14.3	16.4	13.1	10.5
$10l$-$13m$	18.4	24.3	24.7	22.9	25.2	19.3	15.1
$10m$-$13n$	11.1	16.6	19.3	22.3	23.3	18.4	15.0
Sum2	60.5	74.1	74.6	67.7	72.0	57.6	46.2
Sum1 + Sum2	207.5	261.5	273.2	286.2	299.8	261.8	222.3
$9h$-$12i$	11.1	9.9	8.7	7.0	6.6	6.6	5.6
$9i$-$12k$	21.7	20.7	19.5	15.5	17.4	15.4	12.0
$9k$-$12l$	29.0	30.8	29.8	29.0	32.1	26.2	21.1
$9l$-$12m$	22.5	27.8	29.2	33.7	34.6	28.4	22.8
Sum	84.1	89.2	87.2	85.2	90.7	76.6	61.5
$10i$-$12k$	21.0	20.1	18.9	15.1	16.9	15.0	11.6
$10k$-$12l$	36.2	38.4	37.2	36.2	40.1	32.7	26.4
$10l$-$12m$	48.1	59.4	62.3	71.9	73.9	60.7	48.7
$10m$-$12n$	45.0	64.5	71.2	92.1	88.3	77.9	69.8
Sum	150.3	182.4	189.6	215.3	219.2	186.3	156.5
$11k$-$14l$	3.2	5.2	5.8	4.7	5.3	5.5	5.0
$11l$-$14m$	3.1	5.4	7.1	6.8	8.5	8.7	7.6
$11m$-$14n$	1.9	4.6	6.5	7.7	11.2	9.8	9.9
$11n$-$14o$	0.6	2.0	3.7	6.2	8.6	8.0	8.6
Sum	8.8	17.2	23.1	25.4	33.6	32.0	31.1

$\sigma_{6p_i}(10\ell$-$12\ell')$, and $\sigma_{6p_i}(9\ell$-$11\ell'+10\ell$-$13\ell')$ ($i\equiv\Sigma,\Pi$) cross sections are almost constant over all the energy range.

Concerning the $\{9\ell$-$11\ell'+10\ell$-$13\ell'\}$ group of lines that could not be resolved in the experiment, the CTMC calculated emission cross sections corresponding to the 9ℓ-$11\ell'$ and 10ℓ-$13\ell'$ groups of lines are shown in Fig. 6(b). Because of the fair agreement observed between the experimental and theoretical data (Tables II and V), we can reasonably think that the CTMC calculated emission cross sections give a good picture of the reality. Thus we can conclude from Fig. 6(c) that the $\sigma_{6p_i}(9\ell$-$11\ell'+10\ell$-$13\ell')$ ($i\equiv\Sigma,\Pi$) experimental emission cross sections are mainly due to the contributions of the $\sigma_{6p_i}(9\ell$-$11\ell')$ ($i\equiv\Sigma,\Pi$) emission cross sections. Moreover, the CTMC calculations indicate that the 11ℓ states are both populated by direct capture and important radiative cascade effects from upper levels $n=12$ to 14.

Concerning the 11ℓ-$14\ell'$ group of lines [Fig. 6(c)], it is important to note that the $\sigma_{6p_i}(11\ell$-$14\ell')$ ($i\equiv\Sigma,\Pi$) emission cross sections have the same behavior with energy as the $\sigma_{6s}(9\ell$-$11\ell')$ emission cross sections observed in Ar^{8+}-Cs($6s$) collisions [1]. As discussed later on, the population of the highest 14ℓ angular momentum is very weak at low energy and increases quickly with the projectile velocity, similar to the highest 11ℓ angular momentum in the case of Ar^{8+}-Cs($6s$) collisions. The cascade effects being negligible in both cases, the emission cross sections for these lines increase quickly with energy.

Taking into account the uncertainties, no experimental anisotropy can be shown for the studied lines. This result is in agreement with the CTMC calculations that do not predict any anisotropy effect in the 0.4–4.0 keV/amu energy range. All these results confirm those reported by Schippers *et al.* [22] in a comparative study of He^{2+}, O^{4+}, and O^{6+}-Na($3p$) systems: when the size and the charge of the projectile in-

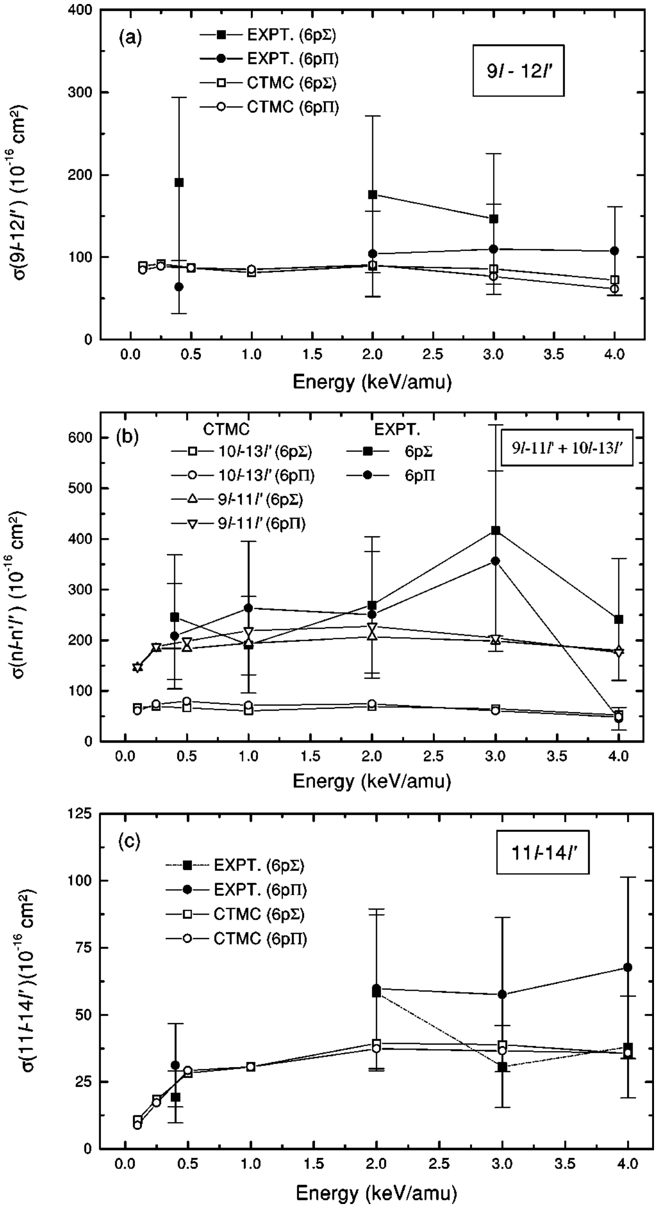

FIG. 6. Comparisons between experimental (full symbols) and CTMC calculated (open symbols) emission cross sections versus the collision energy for $9\ell-12'$ (a), $\{9\ell-11\ell'+10\ell-13\ell'\}$ (b), and $11\ell-14\ell'$ transitions (c).

TABLE VI. Experimental polarization rates (%) versus the projectile energy (keV/amu) for single electron capture in Ar^{8+}-Cs($6s$,$6p\Sigma$) and Ar^{8+}-Cs($6s$,$6p\Pi$) collisions (see text).

	Ar^{8+}-Cs($6s$,$6p\Sigma$) collisions				
Energy	0.4	1.0	2.0	3.0	4.0
$8g$-$9h$	20.2 ± 1.1		20.6 ± 4.6	25.8 ± 4.1	16.7 ± 3.0
8ℓ-$9\ell'$	19.8 ± 1.2		29.4 ± 1.6	28.9 ± 1.6	29.7 ± 1.0
8ℓ-$10\ell'$			25.7 ± 4.6	30.0 ± 3.4	29.5 ± 2.5
10ℓ-$12\ell'$	17.2 ± 1.9		23.9 ± 3.9	30.4 ± 5.3	30.2 ± 5.0
10ℓ-$13\ell'+9\ell$-$11\ell'$	22.4 ± 3.8		28.8 ± 0.7	28.5 ± 2.0	29.9 ± 1.7
	Ar^{8+}-Cs($6s$,$6p\Pi$) collisions				
Energy	0.4	1.0	2.0	3.0	4.0
$8g$-$9h$	16.7 ± 3.5	12.4 ± 3.5	21.5 ± 2.1	23.9 ± 1.4	22.9 ± 1.9
8ℓ-$9\ell'$	19.1 ± 1.5	29.9 ± 1.6	28.1 ± 2.1	28.7 ± 1.3	28.4 ± 1.2
8ℓ-$10\ell'$	20.0 ± 7.5	25.8 ± 9.1	28.4 ± 2.7	24.8 ± 6.3	24.1 ± 4.3
10ℓ-$12\ell'$	17.5 ± 1.8	19.6 ± 5.3	22.3 ± 3.6	32.6 ± 4.3	29.3 ± 3.3
10ℓ-$13\ell'+9\ell$-$11\ell'$	19.1 ± 2.5	29.9 ± 0.7	28.1 ± 1.9	28.7 ± 3.7	28.4 ± 2.0

crease, the anisotropy decreases because the electron capture takes place at larger internuclear distances. The projectile ion is then less sensitive to the initial preparation state of the target.

In conclusion, in spite of experimental difficulties [very weak excited caesium fraction, stability of laser diodes, geometry of the experiment (three beams crossing over)], $\sigma_{6p_i}(9\ell\text{-}12\ell')$, $\sigma_{6p_i}(10\ell\text{-}12\ell')$, $\sigma_{6p_i}(9\ell\text{-}11\ell'+10\ell\text{-}13\ell')$, and $\sigma_{6p_i}(11\ell\text{-}14\ell')$ $(i\equiv\Sigma,\Pi)$ emission cross sections are in good agreement with CTMC calculations for the absolute values of the emission cross sections and for the absence of anisotropy.

C. Polarization degrees of lines

The polarization degrees P of the 8ℓ-$9\ell'$, 8ℓ-$10\ell'$, and 10ℓ-$12\ell'$ groups of lines and those of the $\{9\ell\text{-}11\ell'+10\ell\text{-}13\ell'\}$ mixing of lines have been determined in the 0.4–4.0 keV/amu energy range. They are reported in Table VI. As in Ar^{8+}-Cs($6s$) collisions [1], it was only possible to determine P for transitions whose intensities are enough important, that means for transitions between states with large ℓ values. Moreover, because the cesium target is not completely excited, the measured polarization degrees correspond respectively to Ar^{8+}-Cs($6s$,$6p_\parallel$) and Ar^{8+}-Cs($6s$,$6p_\perp$) collisions. The polarization rate P being defined as

$$P=\frac{I_\parallel-I_\perp}{I_\parallel+I_\perp}, \tag{15}$$

it is very difficult to separate the polarization rates corresponding to Ar^{8+}-Cs($6s$) collisions from the ones corresponding to Ar^{8+}-Cs($6p_\parallel$) collisions [respectively, Ar^{8+}-Cs($6p_\perp$) collisions]. Note also that since the anisotropy is found to be zero or almost zero, it was not necessary to change the $6p_\parallel$ and $6p_\perp$ initial states of the target into the $6p\Sigma$ and $6p\Pi$ aligned states (this has been verified in the case of the $10h,i,k,l,m$-$12i,k,l,m,n$ group of transitions). Therefore, our experimental results should be compared with CTMC polarization rates corresponding to pure Ar^{8+}-Cs($6s$) and Ar^{8+}-Cs($6p\Sigma$) [respectively, Ar^{8+}-Cs($6p\Pi$)] collisions.

The CTMC calculated polarization degrees are reported in Table VII for Ar^{8+}-Cs($6p\Sigma$) and Ar^{8+}-Cs($6p\Pi$) collisions. The calculations include radiative cascade effects up to $n=14$. The CTMC results are seen to be in fair agreement with the experimental data both for the behavior of the polarization rates versus the collision energy and for their absolute values. The CTMC calculations do not show any alignment effect, in agreement with the experimental results. From these comparisons between CTMC and experimental results, and taking the experimental uncertainties of measured polarization rates into consideration, no significant difference is observed between polarization rates obtained for pure Ar^{8+}-Cs($6s$) and Ar^{8+}-Cs($6p\Sigma$,orΠ) collisions. In the case of Ar^{8+}-Cs($6s$,$6p_\perp$) collisions, the experimental and CTMC calculated polarization degrees of lines versus the collision energy are shown as examples in Figs. 7(a) and 7(b) for the $10h,i,k,l,m$-$12i,k,l,m,n$ and $\{9h,i,k,l\text{-}11i,k,l,m+10i,k,l,m\text{-}13k,l,m,n\}$ groups of lines. Note that, for the clarity of the figures, only CTMC calculated polarization rates corresponding to the borders of groups of transitions considered experimentally have been reported. The CTMC calculated polarization degrees for Ar^{8+}-Cs($6s$) collisions [1] are also shown in the figures. Except for the $9h$-$11i$ transition [Fig. 7(b)], no significant difference is observed between the CTMC calculated polarization rates for the target in the ground state and in the $6p$ excited and aligned state.

The polarization rates are found to be always positive and to increase with the energy from about 15% to values between 25% and 30%. Since the experimental and theoretical data are found in fair agreement, we can say that the CTMC

TABLE VII. CTMC calculated polarization rates (%) versus the projectile energy (keV/amu) for single electron capture in Ar^{8+}-Cs($6p\Sigma$) collisions and Ar^{3+}-Cs($6p\Pi$) collisions.

	Ar^{8+}-Cs($6p\Sigma$) collisions						
Energy	0.1	0.25	0.5	1.0	2.0	3.0	4.0
$8g$-$9h$	15.6	16.7	17.5	15.2	22.5	25.5	26.6
$8h$-$9i$	17.1	18.6	19.1	19.2	25.6	26.5	26.9
$8i$-$9k$	16.9	20.0	20.0	23.1	27.6	27.8	28.1
$8k$-$9l$	13.6	20.1	22.9	26.7	29.6	29.5	29.3
$8h$-$10i$	16.1	17.9	18.0	16.4	24.0	25.7	26.1
$8i$-$10k$	17.3	19.0	19.2	21.3	26.1	26.3	27.0
$8k$-$10l$	16.4	20.4	20.6	24.1	28.1	28.1	26.6
$9h$-$11i$	15.9	15.3	14.9	12.4	22.3	27.2	29.1
$9i$-$11k$	14.8	17.0	17.4	16.7	25.1	26.4	27.9
$9k$-$11l$	15.7	19.0	19.3	22.0	26.5	26.5	28.2
$9l$-$11m$	15.7	20.0	21.4	25.0	28.6	28.6	29.1
$10h$-$12i$	13.8	13.0	16.4	13.6	25.5	30.1	30.6
$10i$-$12k$	17.2	15.9	17.4	16.9	27.8	30.3	29.6
$10k$-$12l$	17.3	18.9	18.7	20.7	28.7	29.1	29.9
$10l$-$12m$	16.4	20.1	20.3	24.4	28.4	29.3	30.2
$10m$-$12n$	15.9	21.4	23.0	27.4	29.8	29.9	30.2
$10h$-$13i$	19.8	21.4	24.3	25.4	25.2	31.6	32.2
$10i$-$13k$	22.2	24.3	25.5	25.4	30.1	32.5	31.9
105-$13l$	24.4	23.2	24.5	26.2	31.5	32.1	31.8
$10l$-$13m$	24.2	25.9	26.1	27.8	32.0	32.4	32.6
$10m$-$13n$	24.9	25.6	25.6	28.9	31.6	32.4	32.2
	Ar^{8+}-Cs($6p\Pi$) collisions						
Energy	0.1	0.25	0.5	1.0	2.0	3.0	4.0
$8g$-$9h$	16.0	16.3	17.3	16.6	21.2	22.0	22.3
$8h$-$9i$	17.6	19.2	20.5	21.4	23.9	24.0	24.1
$8i$-$9k$	18.4	21.3	22.5	24.5	25.8	25.8	25.5
$8k$-$9l$	16.8	21.9	25.2	27.0	27.9	27.7	27.4
$8h$-$10i$	16.9	17.5	18.5	18.7	21.9	22.2	23.1
$8i$-$10k$	17.9	20.2	21.0	22.5	24.5	24.7	24.5
$8k$-$10l$	18.3	21.5	23.2	25.3	26.4	26.1	26.0
$9h$-$11i$	14.5	14.2	15.4	17.1	21.4	23.6	24.8
$9i$-$11k$	15.8	17.8	18.5	20.7	23.7	23.8	25.1
$9k$-$11l$	17.2	20.6	20.9	23.7	24.9	25.5	25.6
$9l$-$11m$	18.0	21.6	23.8	26.2	26.8	26.7	26.8
$10h$-$12i$	13.3	13.6	15.5	17.5	24.9	27.6	26.9
$10i$-$12k$	16.7	16.7	20.2	20.6	25.9	26.6	27.8
$10k$-$12l$	17.9	19.9	20.6	24.0	26.7	27.5	27.9
$10l$-$12m$	18.9	22.2	22.6	25.8	27.2	27.9	28.0
$10m$-$12n$	18.5	23.1	25.2	27.5	28.4	28.4	28.4
$10h$-$13i$	22.1	22.0	24.4	23.3	27.0	30.2	30.8
$10i$-$13k$	23.7	24.0	24.5	25.9	29.5	30.4	30.8
$10k$-$13l$	24.8	25.3	26.9	27.1	30.2	30.5	30.8
$10l$-$13m$	25.0	26.4	27.1	28.6	30.3	30.9	30.5
$10m$-$13n$	25.9	27.1	28.6	29.5	30.3	30.5	30.3

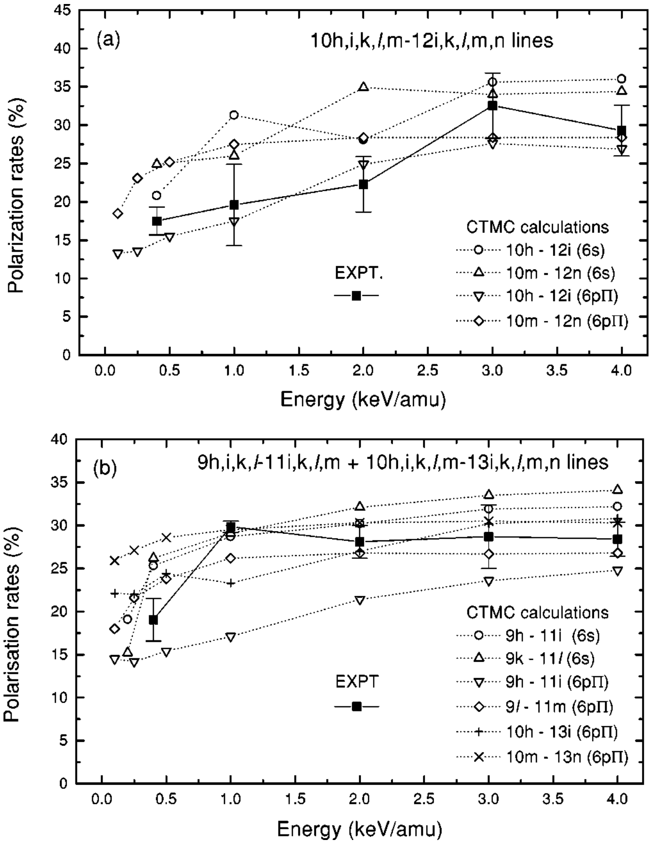

FIG. 7. Comparisons between experimental (full squares) and theoretical (open symbols) polarization degrees of the lines for the $10h,i,k,l,m$-$12i,k,l,m,n$ (a) and $\{9h,i,k,l$-$11i,k,l,m + 10i,k,l,m$-$13k,l,m,n\}$ transitions (b). The experimental polarization rates are reported for Ar^{7+}-Cs($6s$,$6p\Pi$) collisions, while the CTMC calculated rates for individual transitions are reported for pure Ar^{7+}-Cs($6s$) and Ar^{7+}-Cs($6p\Pi$) collisions (see text).

$n\ell m_\ell$ distributions give a good picture of the reality for the studied transitions. Therefore, as previously concluded from our study of Ar^{8+}-Cs($6s$) collisions [1], the magnetic sublevels of $m_\ell \leqslant 4$ are mainly populated at the highest energies, whereas most of the m_ℓ sublevels are populated when the energy decreases.

V. MOLECULAR ANALYSIS OF THE STATE-SELECTIVE ELECTRON CAPTURE

Details of electronic-energy calculations for the one-electron $\{\mathrm{Ar}^{7+}+\mathrm{Cs}\}^{+}$ system have been already reported [1]. These calculations are based on a pseudopotential method and use a linear combination of numerical atomic orbitals for the Cs atom and the Ar^{7+} ion [38]. The electronic energies can be calculated for various symmetries Λ of the molecular system, where Λ is the absolute value of the projection of the total orbital momentum of the system along the internuclear axis (taken as the quantization axis). They allow us to discuss CTMC and experimental results of state-selective electron capture in terms of dynamical couplings: radial couplings between molecular states with $\Delta\Lambda = 0$ and rotational couplings with $\Delta\Lambda = \pm 1$. In order to discuss the

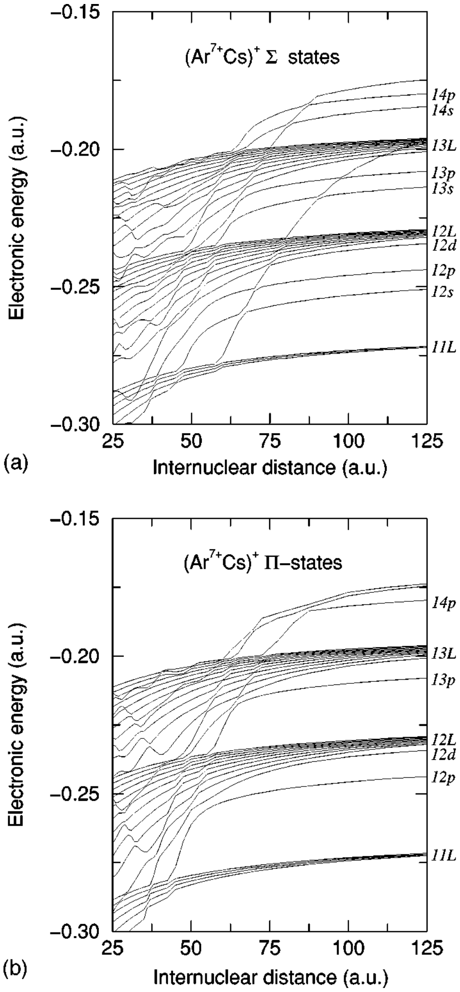

FIG. 8. Electronic energies (in atomic units) versus the internuclear distance (in atomic units) for the $\{Ar^{7+}+Cs\}^+$ system. (a) Σ states, (b) Π states.

Ar^{8+}-Cs($6p\Sigma$ or Π) collisions, the electronic energies for the $\Lambda=0$ and 1 symmetries (i.e., the Σ and Π molecular states) are reported in Figs. 8(a) and 8(b), for the $R=25-125$ a.u. internuclear distance range. They are centered on the main capture channels corresponding to the $n=12$ and 13 levels of Ar^{7+}.

In Ar^{8+}-Cs($6s$) collisions, or more generally for collisions between an Ar^{8+} ion and an alkali-metal atom target in its ground state, the only entrance channel is a Σ molecular state. However, in the case of a Cs target excited in a $6p\Sigma$ or $6p\Pi$ aligned state, the entrance channel may have two possible symmetries: a Σ state for a Cs($6p\Sigma$) target and a Π state for a Cs($6p\Pi$) target. In Fig. 8(a), the $\Sigma(6p)$ entrance channel corresponds to the second Σ energy curve above the manifold of electronic-energy curves correlating to the $n=11$ level of Ar^{7+}; it emerges at $R\approx75$ a.u. from the manifold of curves corresponding to the $n=13$ level after undergoing numerous avoided crossings or nearly diabatic crossings with the electron-capture molecular channels. Then, this entrance channel goes, through numerous nearly diabatic crossings, to the $6p\Sigma$ state of Cs at large internuclear distances. Note that the first Σ energy curve above the $n=11$ manifold of curves and going through the manifold of molecular states corresponding to the $n=12$ and 13 levels is the entrance channel for a Cs($6s$) target. In Fig. 8(b) the $\Pi(6p)$ entrance channel is the first Π energy curve above the manifold of states corresponding to $n=11$ level of Ar^{7+} and that emerges at $R\approx72.5$ a.u. from the manifold of states corresponding to the $n=13$ level. This entrance channel goes through numerous nearly diabatic crossings to the $6p\Pi$ state of Cs at large R values. In the first place, the sets of energy curves (Σ or Π) correlating to the $n=12$ and 13 levels show a similar behavior than the sets of energy curves of same symmetry correlating to the main populated levels ($n=9$ and 10) in Ar^{8+}-Cs($6s$) collisions (see Fig. 2 of Ref. [1]). So, we can reasonably assume that the coupling mechanisms for populating the $n=12$ and 13 levels in Ar^{8+}-Cs($6p\Sigma$,orΠ) collisions should be similar to those populating the $n=9$ and 10 levels in Ar^{8+}-Cs($6s$) collisions [1]. In the second place, the Σ or Π molecular channels for electron capture into the $n=12$ and 13 levels of Ar^{7+} exhibit about similar avoided crossings with the entrance channel of same symmetry for the low ℓ sublevels of each manifold n (except that for the Π

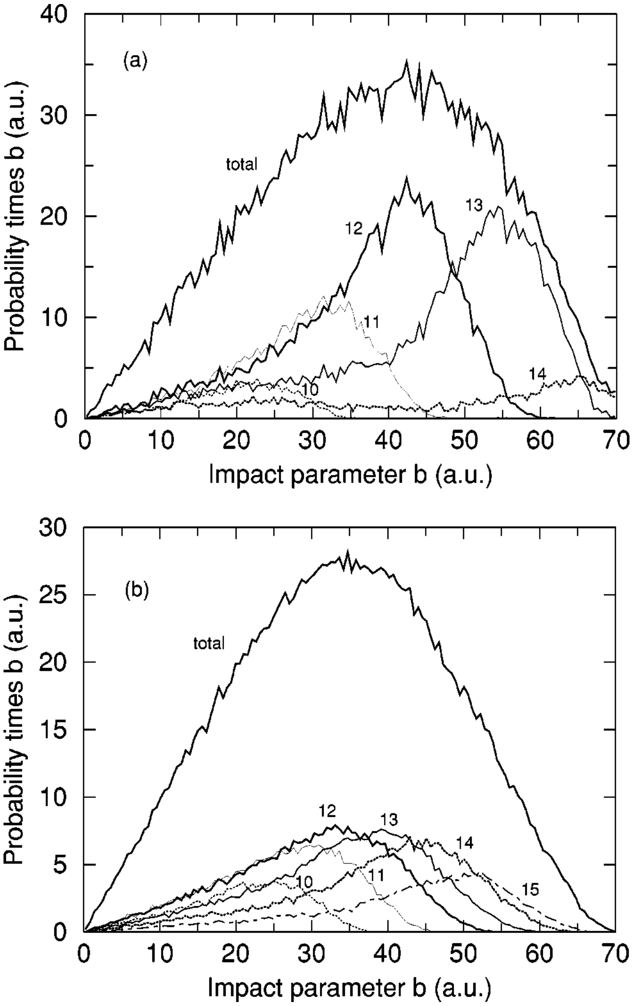

FIG. 9. CTMC calculated probability times b versus impact parameter b for total electron capture and electron capture into n levels of Ar^{7+} from Cs($6p\Pi$) (as indicated in the figure), at projectile energies of 0.25 keV/amu (a) and 4 keV/amu (b).

molecular states, the energy splitting at the avoided crossings are comparatively a little smaller than for the Σ molecular states). So, on the whole, the cross sections for electron capture into the $n\ell$ sublevels of Ar^{7+} from $\mathrm{Cs}(6p\Sigma)$ and $\mathrm{Cs}(6p\Pi)$ targets should vary similarly with the projectile energy.

As seen in Fig. 8(a) the $\Sigma(6p)$ entrance channel crosses nearly diabatically the manifold of $\Sigma_{n\ell}$ $(\ell>3)$ exit channels correlating to the 12ℓ and 13ℓ sublevels of Ar^{7+}. Then, it shows up avoided crossings with $\Sigma_{12\ell}$ and $\Sigma_{13\ell}$ electron capture channels $(\ell<3)$, respectively in the 47–55 a.u. and 60–70 a.u. *R*-value ranges. Similarly, the $\Pi(6p)$ entrance channel exhibits avoided crossings with the $\Pi_{12\ell}$ and $\Pi_{13\ell}$ electron-capture channels $(\ell\leqslant3)$, at approximately the same *R*-value ranges than for the symmetry Σ (i.e., respectively 46–53 a.u. and 60–68 a.u.). In both cases, these avoided crossings are responsible for the primary radial couplings $(\Delta\Lambda=0)$ leading to populate first the low ℓ values of the 12ℓ and 13ℓ sublevels; then, in each *n* manifolds, the population of these low ℓ values is redistributed by successive rotational couplings $(\Delta\Lambda=\pm1)$ and Stark effect of the residual Cs^{+} ion. As examples, for Ar^{8+}-$\mathrm{Cs}(6p\Pi)$ collisions and for two projectile energies (0.25 and 0.4 keV/amu), Figs. 9(a) and 9(b) show that the maximum impact parameter *b* that contributes to the total electron-capture cross section and to the electron capture into predominantly populated *n* levels agrees with the *R*-value ranges of the primary radial couplings.

At the highest energies, the intrashell rotational couplings and the Stark effect of the residual Cs^{+} ion are important, so that, large values of ℓ are mostly populated. When the energy decreases, the rotational couplings become less important while the primary radial couplings that populates the low ℓ values become successively more and more efficient at low energies (beginning with those relating to avoided crossings with the largest energy splittings). As a consequence, the population of the highest ℓ values decreases more or less at the benefit of the lowest ℓ values (this is the so-called projectile core-electron effect). Figures 10(a) and 10(c) show such a behavior with the projectile energy of the CTMC calculated cross sections for electron capture into the 12ℓ and 13ℓ sublevels. Note that, as for electron capture into the 9ℓ and 10ℓ sublevels in Ar^{8+}-$\mathrm{Cs}(6s)$ collisions [1], the CTMC calculated 12ℓ and 13ℓ distributions go through a maximum for $l=1$ at low energies, but these maxima take a larger value than for the largest ℓ values of the distributions for a projectile energy smaller than ≈0.1 keV/amu only, when it is smaller than ≈0.4 keV/amu for a $\mathrm{Cs}(6s)$ target because, in this case, of larger-energy splittings at the involved avoided crossings.

Similar variations of the $n\ell$ distributions with the projectile energy are also observed for $n=11$ [Fig. 10(c)] and for $n=14$ [Fig. 10(c)], but with some appreciable changes. In the case of the 11ℓ distributions, the core-electron effect is still quite important and the maxima at the low ℓ values are the largest for $\ell=1$ at energies ≈0.25–1 keV/amu for the $\mathrm{Cs}(6p\Sigma)$ target, while the 11ℓ distribution exhibits a broad maximum centred on $\ell=2$ at 0.1 keV/amu. For the $\mathrm{Cs}(6p\Pi)$ target, the maximum of the distribution for $\ell=2$ at 0.1 keV/amu takes a value as large than the maxima of the distributions for $\ell=1$ at 0.25 and 0.5 keV/amu. This may be attributed to larger-energy splittings at the avoided crossings involved in the electron capture into the 11ℓ sublevels, in comparison with those involved in the capture into higher $n\ell$ sublevels. Relating to this, it is interesting to remark that the maximum at low energies in the 12ℓ distribution is already appreciably broadened with respect to that in the 13ℓ distribution. We can consider, however, that the coupling mechanisms for populating the 11ℓ sublevels are the same than those for populating the 12ℓ and 13ℓ sublevels. As seen in Fig. 10(c) the low values of ℓ in the 14ℓ distributions become more and more populated with decreasing energies (but without taking values as large than those of the largest ℓ values at large energies), at the detriment of the largest values of ℓ. This particular behavior of the state-selective $n\ell$ distribution has been pointed out already for the 11ℓ distribution in the case of Ar^{8+}-$\mathrm{Cs}(6s)$ collisions [1]. Therefore, as in Ref. [1], primary intershell rotational couplings between the entrance channel $\Sigma(6p)$ and Π exit channels, and between the $\Pi(6p)$ entrance channel and Σ or Δ exit channels, have to be invoked to populate the low ℓ values of the $n=14$ level (and also, other higher *n* levels). This is substantiated by the fact that, above the manifold of energy curves correlating to the $n=13$ level of Ar^{7+}, the $\Sigma(6p)$ and $\Pi(6p)$ entrance channels cross nearly diabatically the electron-capture molecular channels of same symmetry. In addition, as expected from our study on Ar^{8+}-$\mathrm{Cs}(6s)$ collisions [1], the CTMC calculated cross sections for electron capture into the *n* levels $(n\geqslant14)$ are found to increase continuously with increasing energy due to more efficient rotational couplings, while the cross sections for electron capture into the $n=12$ and 13 levels decrease quickly (this can be seen in Fig. 5).

The anisotropy parameters, defined as [39]

$$A(n\ell)=\frac{\sigma_{6p\Sigma}(n\ell)-\sigma_{6p\Pi}(n\ell)}{\sigma_{6p\Sigma}(n\ell)+\sigma_{6p\Pi}(n\ell)}, \tag{16}$$

measure the influence of the alignment of the excited Cs target on the state-selective electron capture into the $n\ell$ sublevels of Ar^{7+}. The $A(n\ell)$ parameters have been calculated from the CTMC calculated cross sections for electron capture into the $n\ell$ sublevels for the most populated levels $(n=11–14)$, in the 0.1–4 keV/amu energy range. In general, the variations with the projectile energy of the anisotropy parameter are quite different of one another. For example, the $A(12\ell)$ anisotropy parameters are found to vary much for energies above 0.5 keV/amu, for the lowest and largest values of ℓ, while at the lowest energies they all take small values. Thus, the $A(12s)$ anisotropy parameter is nearly equal to +0.4 at energies of 1 and 2 keV/amu; it takes nearly a 0 value at 0.1 keV/amu and a value of ≈0.2 at 4 keV/amu. More generally, it is found that the Σ alignment influences strongly the lowest ℓ values of the $n\ell$ distribution, while the largest ℓ values are on the whole influenced by the Π alignment. This can hardly be deduced from Figs. 10(a) and 10(c). As the radiative cascade from upper levels do not contribute

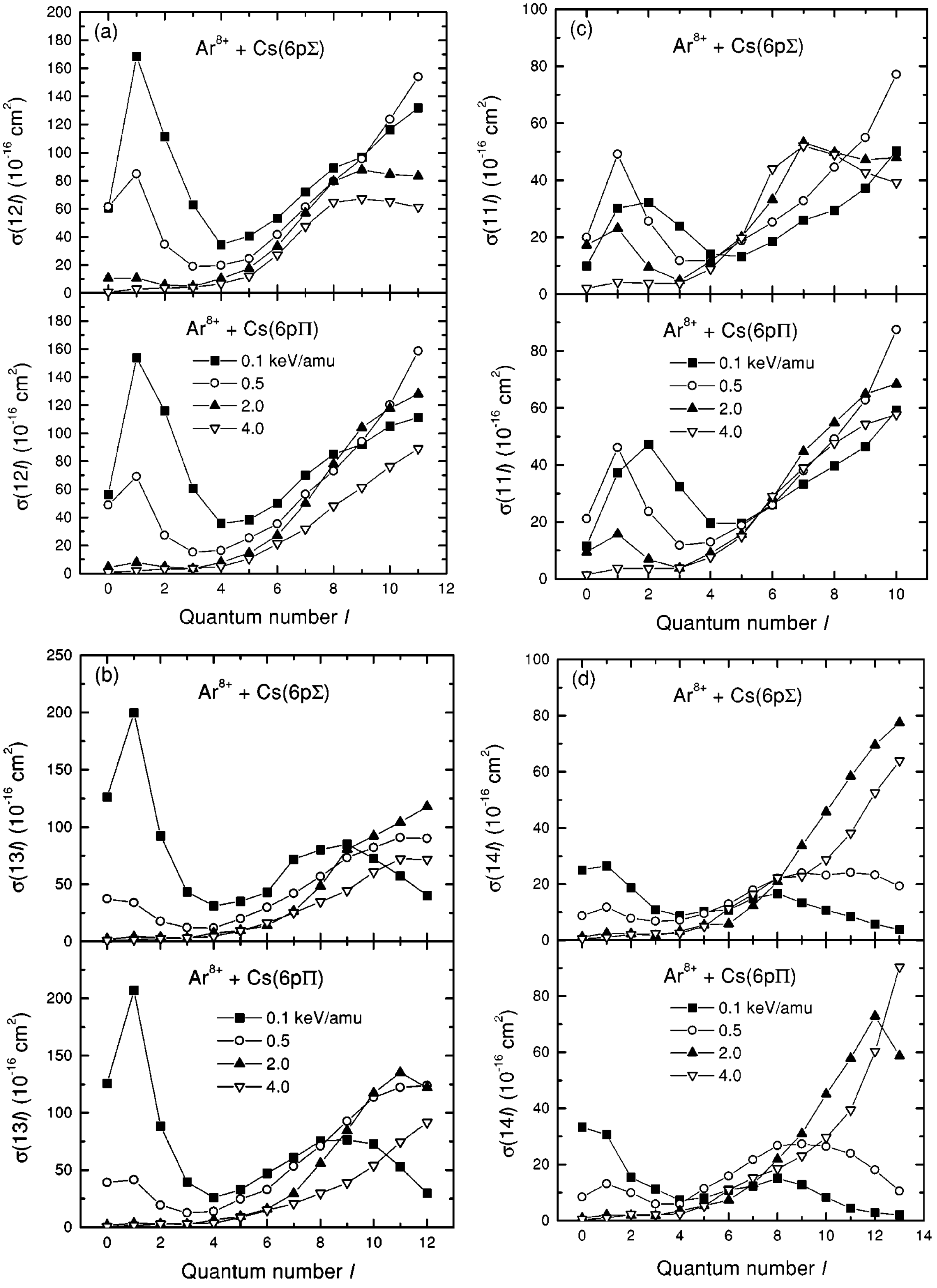

FIG. 10. CTMC calculated $\sigma(n\ell)$ electron-capture cross section versus the angular momentum ℓ at various projectile energies (as indicated in the figure) for $n=12$ (a), $n=13$ (b), $n=11$ (c), and $n=14$ (d).

much to line-emission cross sections for transitions from the 12ℓ levels, this fact could be deduced from the results reported in Tables IV and V. However, since the experiment could not discriminate between the individual transitions, we have judged useless to discuss further the anisotropy parameter. In conclusion, except a few cases, the CTMC calculated electron-capture cross sections for the Σ and Π aligned states do not show any significant difference to be appreciated experimentally. The changes in the calculated cross sections are generally much smaller than the experimental uncertainties. It is interesting to note, however, that in general the CTMC calculations find that the electron capture into the $n\ell$ sublevels present large differences whether the electron capture is from $6p\Pi^+$ initial state or from a $6p\Pi^-$ initial state. This was already pointed out in Ref. [18], where the electron-capture cross section into the dominant final state from a $np\Pi^+$ initial state was found generally larger than from a $np\Pi^-$ initial state. In the present CTMC calculations, however, the electron capture is found predominant also from a $6p\Pi^-$ initial state for capture into $n\ell$ sublevels with the largest ℓ values; it is generally found predominant from a $6p\Pi^+$ initial state for capture into $n\ell$ sublevels with the lowest ℓ values.

Concerning the m_ℓ distributions, the decrease of the polarization rates with the projectile energy indicates that the electronic cloud has more time to adjust itself adiabatically to the rotation of the internuclear axis. Therefore, the m_ℓ distributions are more sensitive to the radial couplings, that is to the projectile core-electron effect. In other words, the rotational couplings become less efficient, in particular, the intershell rotational couplings (i.e., for $\Delta\ell\neq 0$). Only the intrashell rotational couplings (i.e., for $\Delta\ell=0$) remain possible, leading to an intrashell broadening of the m_ℓ distributions among a $n\ell$ sublevel. This was discussed in details elsewhere (see, Refs. [38,40]).

VI. CONCLUSION

Experimental and theoretical study of Ar^{8+}-$Cs(6p\Sigma)$ and Ar^{8+}-$Cs(6p\Pi)$ collisions between 0.1 and 4.0 keV/amu brings insight on the single-electron-capture process. From a spectroscopic point of view, three more lines corresponding only to transitions between large ℓ values have been identified. From lines intensities, the emission cross sections corresponding to the most populated levels ($n=11$ to 14) have been determined and compared with CTMC calculations. In general a fair agreement is found, taking into account the experimental uncertainties. In particular, the experiment and the CTMC calculations both indicate that there is no appreciable anisotropy effect. This result confirms the findings of Schippers *et al.* [22] in a comparative study of He^{2+} C^{4+}, and $O^{5+}-Na(3p)$ systems. When the size and the charge of the projectile increase, the anisotropy parameter decreases and is nearly equal to 0. At large internuclear distances, the projectile ion is almost not sensitive to the initial alignment of the laser-prepared target. Our results have been analyzed in terms of dynamical couplings from calculations of electronic energies for the one-electron $\{Ar^{7+}\text{-}Cs\}^+$ system. The measurements of the polarization degrees of Ar^{7+}-ion emission lines corresponding to transitions between large-ℓ values have been realized experimentally and compared with theoretical ones obtained from CTMC calculated $\sigma(n\ell m_\ell)$ cross sections in Ar^{8+}-$Cs(6s)$ and Ar^{8+}-$Cs(6p\Sigma \text{or} \Pi)$ collisions. The polarization rates increase with the projectile energy. In other words, after the collision, the electronic cloud tends to be more aligned parallel to the incident ion beam: the m_ℓ distribution of the $n\ell$ produced states is more and more peaked on low m_ℓ values. Moreover, this effect does not seem to depend on the initial alignment of the laser-prepared target.

ACKNOWLEDGMENTS

The authors would like to thank Dr. L. Féret for spectroscopic calculations of high-energy levels of the Ar^{7+} ion from a relativistic semiempirical pseudopotential approach. Electronic energy and CTMC calculations were performed on Cray 94 at CEA Saclay under Project No. P65. It is a pleasure to acknowledge the staff of the GANIL test bench for their efficient support.

---

[1] V. Bazin, P. Boduch, M. Chantepie, G. Cremer, E. Jacquet, H. Kucal, D. Lecler, and J. Pascale, Phys. Rev. A **62**, 052706 (2000).

[2] D. Dijkkamp, A. Brazuk, A. G. Drentje, F. J. De Heer, and H. Winter, J. Phys. B **17**, 4371 (1984).

[3] D. M. Gauntt and K. Danzmann, Phys. Rev. A **46**, 5580 (1992).

[4] R. Abrines and I. C. Percival, Proc. Phys. Soc. London **88**, 861 (1966).

[5] R. Abrines and I. C. Percival, Proc. Phys. Soc. London **88**, 873 (1966).

[6] R. E. Olson and A. Salop, Phys. Rev. A **16**, 531 (1977).

[7] R. Witte, E. E. B. Campbell, C. Richter, H. Schmidt, and I. V. Hertel, Z. Phys. D: At., Mol. Clusters **5**, 101 (1987).

[8] E. Campbell, R. Witte, and I. Hertel, J. Phys. B **24**, 4245 (1991).

[9] D. Dowek, J. C. Houver, J. Pommier, C. Richter, and T. Royer, Phys. Rev. Lett. **64**, 1713 (1990).

[10] Z. Roller-Lutz, Y. Wang, K. Finck, and H. O. Lutz, J. Phys. B **26**, 2697 (1993).

[11] J. W. Thomsen, N. Andersen, D. Dowek, J. C. Houver, M. O. Larsson, J. H. V. Lauritsen, U. Müller, J. O. P. Pedersen, J. Salgado, and A. Svenssen, J. Phys. B **28**, L93 (1995).

[12] F. Aumayr, M. Gieler, J. Schweintzer, H. Winter, and P. Hansen, Phys. Rev. Lett. **68**, 3277 (1992).

[13] M. Gieler, F. Aumayr, J. Schweinzer, W. Koppensteiner, W. Husinsky, K. Lozhkin, and J. P. Hansen, J. Phys. B **26**, 2137 (1993).

[14] A. R. Schlatmann, thesis, Groningen, 1993.

[15] S. Schippers, A. R. Schlatmann, and R. Morgenstern, Phys. Lett. A **181**, 80 (1993).

[16] M. Gieler, F. Aumayr, M. Weber, H. P. Winter, and J. Schwein-

zer, J. Phys. B **26**, 2153 (1993).

[17] A. N. Perumal and D. N. Tripathi, Eur. Phys. J. D **8**, 169 (2000).

[18] F. Aumayr, M. Gieler, H. Winter, and J. Schweintzer, J. Phys. B **29**, 1515 (1996).

[19] S. Maleki, M. L. A. Raphaelian, M. P. Stöckli, B. P. Walch, and B. D. DePaola, Phys. Rev. A **48**, 1185 (1993).

[20] B. P. Walch, S. Maleki, R. Ali, M. P. Stöckli, M. L. A. Raphaelian, C. L. Cocke, and B. D. DePaola, Phys. Rev. A **47**, R3499 (1993).

[21] S. Schippers, A. R. Schlatmann, W. P. Wiersema, R. Hoekstra, and R. Morgenstern, Phys. Rev. Lett. **72**, 1628 (1994).

[22] S. Schippers, R. Hoekstra, R. Morgenstern, and R. E. Olson, J. Phys. B **29**, 2819 (1996).

[23] A. R. Schlatmann, R. Hoekstra, and R. Morgenstern, Phys. Rev. Lett. **71**, 513 (1993).

[24] D. Dowek, J. C. Houver, I. Reiser, J. Salgado, A. Svensson, and J. W. Thomsen, Phys. Rev. A **54**, 970 (1996).

[25] D. Dowek and J. C. Houver, Nucl. Instrum. Methods Phys. Res. B **124**, 232 (1997).

[26] J. Taylor and I. Langmuir, Phys. Rev. **44**, 423 (1933).

[27] C. Laulhé, E. Jacquet, P. Boduch, M. Chantepie, N. Gherardi, X. Husson, D. Lecler, and J. Pascale, J. Phys. B **30**, 2899 (1997).

[28] H. Meijer, Thesis, Utrecht, 1988.

[29] S. Svanberg and G. Belin, Z. Phys. **251**, 1 (1972).

[30] W. Demtröder, *Laser Spectroscopy (Basic Concepts and Instrumentation)* (Springer Verlag, Berlin, 1988), p. 472.

[31] A. C. G. Mitchell and M. W. Zemansky, *Resonance Radiation and Excited Atoms* (Cambridge University Press, Cambridge 1961), p. 146.

[32] U. Fano and J. H. Macek, Rev. Mod. Phys. **45**, 553 (1973).

[33] C. O. Reinhold and C. A. Falcón, Phys. Rev. A **33**, 3859 (1986).

[34] A. Lindgård and S. E. Nielsen, At. Data Nucl. Data Tables **19**, 533 (1977).

[35] R. D. Cowan, *The Theory of Atomic Structure and Spectra* (University of California, Berkeley, 1981).

[36] L. Féret and J. Pascale, J. Phys. B **32**, 4175 (1999).

[37] P. Boduch, M. Chantepie, D. Hennecart, X. Husson, H. Kucal, D. Lecler, and N. Stolterfoht, Phys. Scr. **45**, 204 (1992).

[38] C. Laulhé, E. Jacquet, G. Cremer, J. Pascale, P. Boduch, G. Rieger, M. Chantepie, and D. Lecler, Phys. Rev. A **55**, 1088 (1997).

[39] A. Fischer and I. V. Hertel, Z. Phys. A **304**, 103 (1982).

[40] E. Jacquet, H. Kucal, V. Bazin, P. Boduch, M. Chantepie, G. Cremer, C. Laulhé, and D. Lecler, and J. Pascale, Phys. Rev. A **62**, 022712 (2000).